

MULTI-FAULT ANALYSIS IN INDUCTION MOTORS USING MULTI-SENSOR FEATURES

Xin Xue, V. Sundararajan

Department of Mechanical Engineering, University of California, Riverside

Abstract: This paper reports experimental studies and algorithms to detect three types of faults both individually and in combination in three phase induction motors. The faults studied are 1) eccentricity of the air-gap between the rotor and the stator, 2) damage to the inner/outer race of bearings, and 3) unbalanced resistance of the stator windings. The experiments are conducted under thirteen conditions: the normal no-fault condition, nine single fault conditions and three multiple faults conditions. Two microphones, one vibration sensor and one current sensor are used to collect sound, vibration and current data respectively. The data is analyzed using the Hilbert-Huang transform (HHT) and Fast Fourier Transform (FFT). Features are extracted from the spectrum of intrinsic mode functions and the average value of their envelope for the HHT or just the spectrum of the original signal for the FFT. Three simple classifiers are used to classify these experimental conditions. The results demonstrate that the multiple sensors improve the classification rate and that the Intrinsic Mode Functions obtained by the Hilbert-Huang transform are competitive compared with FFT in classifying multiple faults.

Key Words: Condition Monitoring, Induction Motors, Hilbert-Huang Transform

I. INTRODUCTION

The detection of incipient faults in induction motors has been the subject of research in modeling, fault simulation and feature extraction. Cameron et al [1] derived a characteristic frequency called the principal slot harmonic frequency in current and vibration that result from eccentricity of the air-gap between the stator and the rotor. Dorrell et al [2] observed that low frequency components near the fundamental of the current signal can be used to detect both static and dynamic eccentricity. The characteristic defect frequencies of rolling bearing can appear in the vibration spectrum [3, 4], and in the current spectrum [5].

The technique most frequently used to detect frequencies is the Fast Fourier Transform (FFT). However, this method has a number of deficiencies when directly used over a faulty motor's vibration signature [6]. The FFT

alone is not capable of analyzing the frequency content of a defective bearing signal because such a signal is amplitude-modulated and non-stationary i.e. the characteristics of the signal such as the mean change with time. The wavelet transform is one of the most suitable time-frequency approaches [7, 8]. It however has the disadvantage of a fixed scale frequency resolution [9]. It depends on a single fixed type of mother wavelet chosen arbitrarily. Hilbert-Huang transform (HHT), on the other hand, provides multi-resolution at various frequency scales and takes into consideration- the signal's frequency content and its variation [6, 10]. The implementation of the HHT for bearing fault diagnosis has been reported by Hui and Haiqi [11] and Rai and Mohanty [9]. Hui and Haiqi analyzed the first intrinsic mode function (IMF) of vibration signal and used the spectrum of its envelope to detect the fault defect frequencies. Rai and Mohanty compared the original vibration spectrum of vibration signal and the FFT of the decomposed signals for an outer race fault bearing and an inner race fault bearing. All the characteristic defect frequencies are captured in multiple intrinsic mode functions (IMFs); by contrast some of the characteristic defect frequencies are missing in the original vibration spectrum. Their results suggest that the FFT can be ineffective in the analysis of non-stationary vibration signal from defective bearings and demonstrate that the HHT with FFT of IMFs is an advanced signal processing technique which is necessary for bearing fault diagnosis.

This paper studies the vibration, current and sound signature of an induction motor under 13 conditions – a normal no-fault control condition; three bearing fault conditions: bearing with a scratched inner race, bearing with a scratched outer race and bearing without grease; three air-gap eccentricity conditions: one-side tilted air-gap eccentricity, parallel type air-gap eccentricity, two-side reversed air-gap eccentricity; three unbalanced resistance conditions: phase A with additional resistance, phase B with additional resistance and phase C with additional resistance; three multi-fault conditions: inner race scratched bearing with air-gap eccentricity, outer race scratched bearing with air-gap eccentricity, and unbalanced stator winding resistance with air-gap eccentricity. Section 2 describes the analytical methods used for feature extraction. Section 3 depicts the features extracted from the HHT, FFT and Discrete Wavelet

Transform (DWT) for the study. Section 4 describes the methodology of experiments and Section 5 discusses the results.

II. ANALYTICAL METHODS

1. Fast Fourier Transform (FFT)

FFT is an efficient method to compute the Discrete Fourier Transform (DFT). Let x_0, \dots, x_{N-1} be the time series. The DFT is defined by the formula

$$X_k = \sum_{n=0}^{N-1} x_n e^{-i2\pi k \frac{n}{N}}, \quad k = 0, \dots, N-1$$

For this study, the frequency axis is divided into bins that correspond to frequency zones of interest. The magnitudes of the FFT coefficients in the bins are used as features.

2. Hilbert-Huang Transform (HHT)

Hilbert-Huang Transform is a method to analyze nonstationary and nonlinear time series data in time-frequency-energy representation [12]. HHT is computed in two steps – 1) empirical mode decomposition (EMD) and 2) Hilbert spectral analysis. The HHT uses the EMD to decompose a signal into intrinsic mode functions (IMFs), and then uses the Hilbert transform of the IMFs to obtain instantaneous frequency data.

2.1 Definition of Intrinsic mode functions (IMFs)

Huang et al [12, 13] have defined Intrinsic Mode Functions (IMFs) as a class of functions that satisfy two conditions:

- (1) In the whole data set, the number of extrema and the number of zero-crossings must be either equal or differ at most by one. (In other words, every adjacent local maxima and minima of the wave must cross the zero line.)
- (2) At any point, the mean value of the envelope defined by the local maxima and the envelope defined by the local minima is zero. (In other words, the upper envelope and the lower envelope estimated from the local maxima and local minima are approximately symmetric with regard to the zero line.)

The next section explains the process, called empirical mode decomposition (EMD) to obtain IMFs.

2.2 Empirical mode decomposition

To extract IMFs from the signal $x(t)$, a sifting process comprising the following steps is used:

1) Find the positions and amplitudes of local maxima, and local minima of $x(t)$. Then construct an upper envelope by interpolation (typically a cubic spline interpolation) of the local maxima, and a lower envelope by a similar interpolation of the local minima. Calculate the mean $m_1(t)$ of the upper and lower envelopes. Subtracting the envelope mean signal from the original input signal, we have

$$h_1(t) = x(t) - m_1(t) \quad (1)$$

Check whether $h_1(t)$ meets the requirements to be an IMF as defined in section 2.2.1. If not, treat $h_1(t)$ as new data and repeat the previous process. Then set

$$h_{11}(t) = h_1(t) - m_{11}(t) \quad (2)$$

Repeat this sifting procedure k times until $h_{1k}(t)$ is an IMF as defined in the previous section; this is designated as the first IMF.

$$c_1(t) = h_{1k}(t) \quad (3)$$

2) Subtract $c_1(t)$ from the input signal and define the remainder, $r_1(t)$, as the first residue. Since the residue, $r_1(t)$, still contains information related to longer period components, it is taken as a new data stream. Repeat the above-described sifting process to find more IMFs until the following stopping criteria are met. The sifting process is stopped when either of the following criteria are met: 1) the component $c_n(t)$, or the residue $r_n(t)$, becomes so small in magnitude as to be considered inconsequential, or 2) the residue, $r_n(t)$, becomes a monotonic function from which an IMF cannot be extracted. Finally, the signal can be represented as the sum of IMFs and a residue.

$$x(t) = \sum_{j=1}^n c_j(t) + r_n(t) \quad (4)$$

An example of EMD is shown in Figure 1. The original signal (Figure 1 (a)) is composed of two sinusoidal waves with different frequencies, a triangle wave and a linear trend. The decomposed IMFs and the residue are shown in Figure 1 (b). The decomposed IMF1 and IMF2 represent the signals in higher frequency bands which are very similar to the sine waves of 200 Hz and 40 Hz respectively. The third IMF perfectly matches the triangle wave and the residue corresponds to the linear trend.

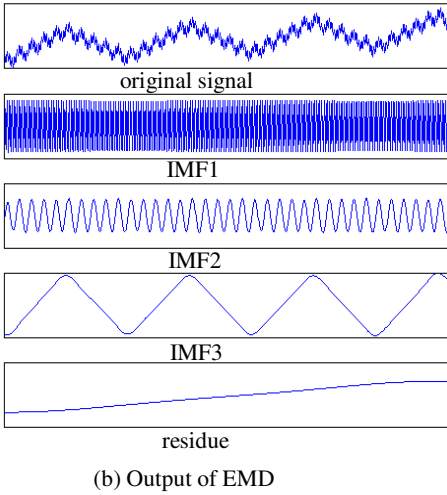
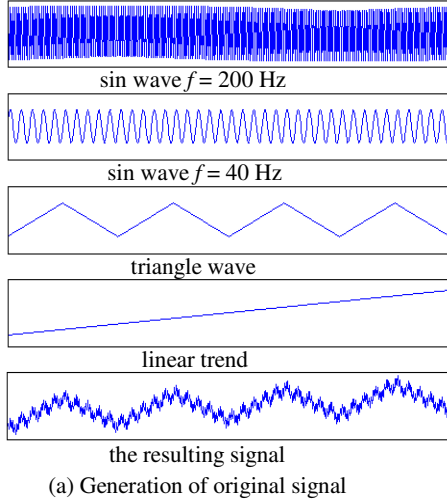


Fig. 1 Example of EMD

(a) Generation of original signal

(b) Output of EMD

2.3 Envelope of IMFs and instantaneous frequency

Apply the Hilbert transform [14] to all the IMFs, $c_j(t)$, we have

$$H[c_j(t)] = \frac{1}{\pi} \int_{-\infty}^{+\infty} \frac{c_j(\tau)}{t-\tau} d\tau \quad (5)$$

A complex signal is formed using the IMF and its Hilbert transform as

$$z_j(t) = c_j(t) + i H[c_j(t)]$$

Expressing $z_j(t)$ in complex exponential form

$$z_j(t) = a_j(t) e^{i\theta_j(t)} \quad (6)$$

where the amplitude of the envelope,

$$a_j(t) = \sqrt{c_j(t)^2 + H[c_j(t)]^2} \quad (7)$$

and the phase angle

$$\theta_j(t) = \arctan\left(\frac{H[c_j(t)]}{c_j(t)}\right) \quad (8)$$

Then the instantaneous frequency is

$$\omega_j(t) = \frac{d\theta_j(t)}{dt} \quad (9)$$

Thus the original signal can be expressed as

$$x(t) = \sum_{j=1}^n a_j(t) e^{i \int \omega_j(t) dt}$$

where the residue has been left out, and the expression represents a generalized Fourier expansion. The average amplitude of the envelope, mean of $a_j(t)$, for certain IMFs will be used as the HHT features. This average amplitude of the envelope is the representation of the energy level of the IMF.

3 Discrete Wavelet Transform (DWT)

Wavelets provide time-scale information of a signal, enabling the information extraction of the signal. The continuous wavelet transform (CWT) of $x(t)$ is a time-scale method of signal processing that is defined by :

$$CWT(a, b) = \frac{1}{\sqrt{|a|}} \int_{-\infty}^{+\infty} x(t) \Psi^*\left(\frac{t-b}{a}\right) dt$$

where $\Psi(t)$ denotes the mother wavelet. The parameter a represents the scale index which is a reciprocal of frequency. The parameter b indicates the time shifting (or translation). The discrete wavelet transform (DWT) is derived from the discretization of CWT (a, b) and the most common discretization is dyadic, given by

$$DWT(l, m) = \frac{1}{\sqrt{2^l}} \int_{-\infty}^{+\infty} x(t) \Psi^*\left(\frac{t-2^l m}{2^l}\right) dt$$

where a and b are replaced by 2^l and $2^l m$. An efficient way to implement this scheme is using high pass and low pass filters developed by Mallat [15]. The original signal, $x(t)$, passes through two complementary filters and emerges as low frequency [approximations (A's)] and high frequency [details (D's)] signals. The decomposition process can be iterated, with successive approximations being decomposed in turn, so that a signal can be broken down into many lower-resolution components. In this study, the vibration signal is decomposed to the first level approximation A1 and detail D1. The current and sound signals are all decomposed to the fifth level approximation A5 and detail D5. Higher level detail signals D3 and D4 are also used since their bandwidths also carry frequencies of interest.

III. FEATURE EXTRACTION

Ideally, even with several faults present in the system, the single fault characteristic frequencies will be present. By inspecting the FFT of each IMF, those fault characteristic

frequencies can be found in the IMFs and the magnitude can be used as features.

1. Bearing Faults Related Frequencies

For a rolling element bearing, the outer/inner race fault characteristic frequencies are [16]:

$$f_o = \frac{n}{2} \left(1 - \frac{d}{D} \cos \beta \right) f_r \quad (10)$$

$$f_i = \frac{n}{2} \left(1 + \frac{d}{D} \cos \beta \right) f_r \quad (11)$$

where n is the number of balls, d is the ball diameter, D is the pitch diameter, β is the contact angle, and f_r is the rotation speed of the rotor. The ball spin frequency is

$$f_{bs} = \frac{D}{d} \left(1 - \left(\frac{d}{D} \cos \beta \right)^2 \right) f_r \quad (12)$$

If a current sensor is used on the supply line or an audio sensor is used to collect the sound signals from the motor, the corresponding current and sound spectra show the fault characteristic frequency [5, 16]

$$f = f_1 \pm f_o \quad (13)$$

where f_1 is the power supply frequency.

2. Air-gap Eccentricity Faults Related Frequencies

For air gap eccentricity fault, the principal slot harmonic (PSH) frequency is calculated by [1, 16]

$$f = \left(\frac{1-s}{p} (kR \pm n_d) \pm v \right) f_1 \quad (14)$$

where s is the slip of the rotor, p is number of pole pairs, R is number of rotor bars, $n_d = 0$ in case of static eccentricity, and $n_d = 1, 2, 3, \dots$ in case of dynamic eccentricity, k is an integer, $v = 1, 3, 5, \dots$. Low frequency components near the fundamental given by [16]

$$f = f_1 \pm k f_r \quad (15)$$

are also related to air-gap eccentricity faults.

Besides the bearing fault characteristic frequency, vibration frequency components due to mechanical faults are also located at the first three harmonics of rotor speed, f_r , $2f_r$, and $3f_r$.

3. Stator Winding Faults Related Frequencies

For stator winding faults, Thomson [17] demonstrated the effectiveness of the current frequency components calculated as follows,

$$f_s = f_1 \left(\frac{n}{p} (1-s) \pm k \right) \quad (16)$$

Where $n = 1, 2, 3, \dots$, $k = 1, 3, 5, \dots$

IV. METHODS

1. Materials

Motor

The experiment setup is shown in Figure 2. The motor used here is a 1.5hp three phase induction motor rated at 230V line voltage and 4.8A line current. It is connected to an adjustable speed drive to control the speed. The running speed of the motor with no load is 1200rpm which corresponds to 20 revolutions per second (20 Hz).

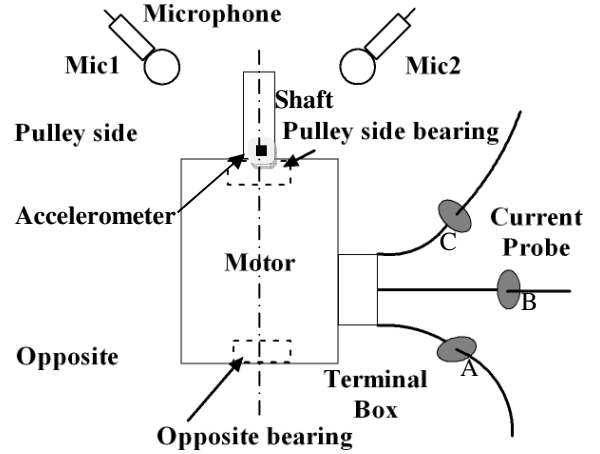


Fig. 2 Experiment setup diagram

Sensors

Current, vibration and sound signals are collected by a current probe, an accelerometer and two microphones respectively. The current probe is an ac current transformer which gives output of 1mA/A AC. The current signal is collected by the data acquisition board using Labview software. The sampling rate for the current probe is set at 8.192 kHz. The accelerometer is commercially available from Crossbow Tech, Inc. The output is a voltage and the sensitivity is 0.506V/g, where g , the earth's gravitational acceleration, is approximately 9.8 m/s². The sampling rate of the accelerometer using the company's hardware and software is 160 Hz. The microphones are connected to the audio analog input on the computer. Sound recording software is used to collect the data. The sampling rate is set to 44.1 kHz. The resulting signal is then down sampled to 8192 Hz.

Conditions

This paper studies the current, vibration and sound signal collected from a 1.5 hp 3-phase induction motor with five categories of conditions (Figure 3) : 1) two-fault condition; 2) unbalanced stator winding resistance; 3) air-gap eccentricity; 4) damaged bearings; 5) normal condition. Except the normal condition, each category contains three sub-classes. The various categories are shown in Figure 3. The two-fault conditions studied are a) damaged bearing with unbalanced stator winding resistance; b) damaged bearing with air-gap eccentricity; c) unbalanced stator winding resistance with air-gap eccentricity. Category 2), 3) and 4) are single fault

conditions. Three phases of stator winding with bigger resistance (approximately 8% larger than the original resistance) are studied as sub-classes. Any two-fault condition involves unbalanced stator winding resistance fault uses an additional resistor for stator phase A winding. The three sub-conditions of air-gap eccentricity are a) one-side tilted type; b) two-side parallel type; c) two-side reversed type. The damaged bearing conditions are inner race scratched, outer race scratched and no grease condition. These will be described in detail.

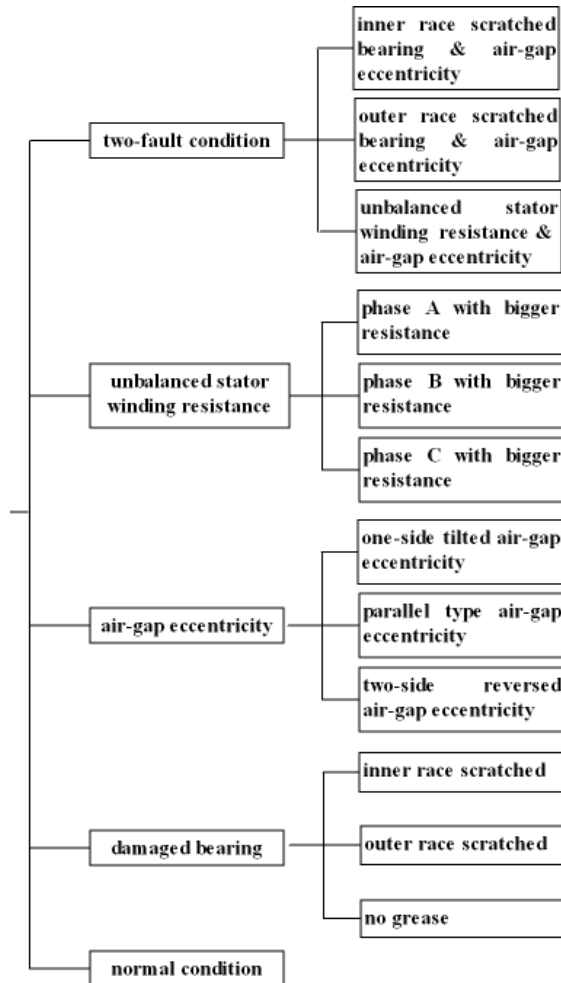


Fig.3 Diagram of induction motor conditions; totally 13 conditions grouped as five categories.

The effects of air-gap eccentricity are studied by replacing the bearings in the motor housing by a smaller outside diameter bearing located in an off-centered bushing (Figure 4). The circled mark point indicates the thickest point of the bushing. The offset causes a deviation of the rotor center line as shown in Figure 5. Three types of air-gap eccentricity are studied. The first one called the one-side tilted air-gap eccentricity replaces only the pulley side bearing (Figure 5(a)). The offset

causes an uneven air-gap length between the rotor and the stator core thus resulting in eccentricity of the air-gap fault. The side view shows the air gap changing linearly between the rotor and stator core along the shaft axis. The second one called the two-side parallel type replaces both the pulley side bearing and the opposite bearing (Figure 5(b)). The center line of the rotor is parallel with the ideal original center line. Both the circled marks of the bushings are placed on bottom. The third one called the two-side reversed type also replaces both the pulley side bearing and the opposite bearing (Figure 5(c)). The difference is to put the circled marks (circled in Figure 4) on opposite sides of the center line. This causes the center line of the rotor to intersect with the original center line only at the mid-point. In Figure 4, L1 is the minimum air gap which is approximately 0.2 mm, and L2 is the maximum air gap which is approximately 0.6 mm. All the two-fault conditions use the one-side tilted type air-gap eccentricity (Figure 5 (a)) which installs the pulley side bearing with its marked side on bottom.

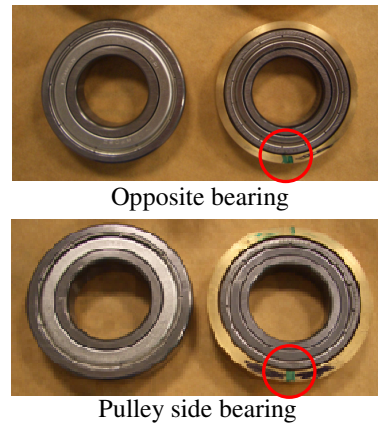
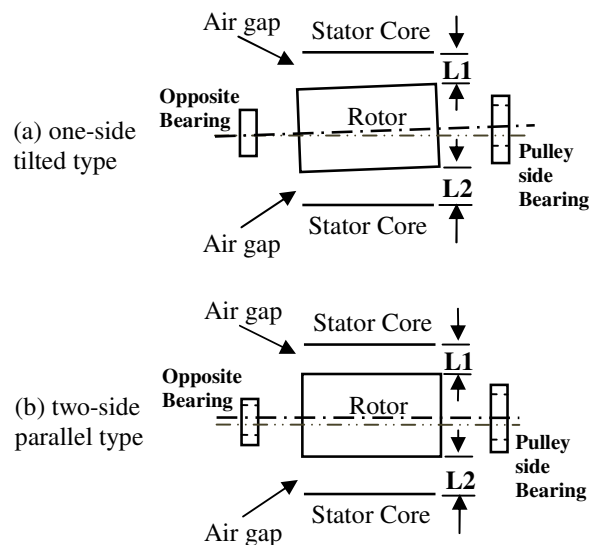


Fig. 4 Original bearings and their replacement, the mark indicates the thickest part of the bushing.



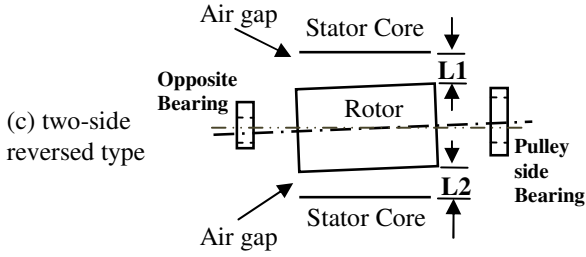


Fig.5 Static air-gap eccentricity

Bearing faults are studied by replacing the opposite bearing of the motor with an open bearing. The open bearing allows access to the race way of a bearing. This bearing is scratched using a diamond mounted tool on the surface of inner/outer race way. The other bearing fault is studied by running the bearing without grease. This will cause damage to both inner and outer race way after some time of running. The two-fault condition of damaged bearing and unbalanced stator winding resistance uses an inner race damaged bearing. The two-fault condition of damaged bearing and air-gap eccentricity uses an outer race damaged bearing.

2. Experimental Design

Experiments are conducted under thirteen different conditions which are grouped as five categories: only bearing fault condition, only air-gap eccentricity condition, only unbalanced stator resistance condition, two faults simultaneously and a normal control condition. For each condition, the motor is set up three times randomly switched from one condition to another. The data are collected in 1 minute time spans and cut to 4 seconds for the vibration signal and 2 seconds for the current and sound signals. The sensor data sets are summarized in Table 1. The sound data are collected at a sampling rate of 44.1 kHz and downsampled to 8192 Hz. The current data is passed through a low pass filter with the cut-off frequency of 1500Hz in order to get rid of the high order harmonics generated by the adjustable speed drive due to pulse width modulation [18]. Current and microphone data frame are set for 2 second durations whereas the accelerometer data is gathered for 4 second durations. For each sensor, 120 sets of data are obtained for each condition except for the normal condition. 360 sets of data are obtained for normal condition and each category has equal number of data sets.

Table 1 Data sets summary

Sensor type	Sampling rate (Hz)	Frame length (second)	No. of frames
accelerometer	160	4	120
Current probe	8192	2	120
Microphone 1	8192	2	120
Microphone 2	8192	2	120

3. Analysis

The Intrinsic Mode Functions (IMFs) are extracted using the procedure outlined in Section 2. Since the sampling rate of the accelerometer is lower, there are fewer features from the vibration sensors. Only two IMFs are used in vibration data, seven IMFs are used in sound, and eight IMFs are used in current data analysis. The frequency components selected from each IMF are based on the fault characteristic frequencies mentioned above. According to the fault related frequencies, the final approximation and several detail signals are used. The mother wavelet used here is Daubechies-4 (db4) [8, 19]. Daubechies wavelet is the most commonly used set of wavelet [19]. The HHT features, FFT features and DWT features selected for different sensors are listed in Table2. The features are then used as input to various two stage classifiers as shown in Figure 6. Half of the data sets are randomly picked as training data. The training data sets are used twice, one for the 5-category classifier, and again for one of the subclass classifiers. The performance is evaluated based on 10 cross validation tests. The details are discussed in the next section.

Table 2 Features List

Vibration data		
HHT features	FFT	DWT
f_r (IMF2), $2f_r$ (IMF1), $3f_r$ (IMF1), f_{bs} (IMF1), f_o (IMF1), IMF1 average envelope, Total: 6	f_r , $2f_r$, $3f_r$, f_{bs} , f_o . Total:5	f_r (A1), $2f_r$ (A1), $3f_r$ (D1), f_{bs} (A1), f_o (D1). Total:5
Current data		
HHT features	FFT	DWT
f_s+f_i (IMF1), PSH (IMF2), $40f_r$ (IMF2), f_s+7f_r (IMF3), f_s+6f_r (IMF3), f_s+6f_r (IMF4), f_s+3f_r (IMF4), f_s-f_i (IMF4), f_s-f_o (IMF4), f_s (IMF5), f_s+3f_r (IMF5), f_s-f_o (IMF8), IMF2 average envelope, Total: 13	PSH, f_1 , f_s+3f_r , f_s+6f_r , f_s+7f_r , f_s+f_i , f_s-f_i , f_s+f_o , f_s-f_o , Total: 9	PSH (D3), f_s (A5), f_s+3f_r (A5), f_s+6f_r (D5), f_s+7f_r (D5), f_s+f_i (D5), f_s-f_i (A5), f_s+f_o (D5), f_s-f_o (A5), Total: 9
Sound data		
HHT features	FFT	DWT
PSH (IMF1), f_s+14f_r (IMF1), f_s+13f_r (IMF2), f_s+12f_r (IMF2), f_s+10f_r (IMF2), f_s+2f_r (IMF3), f_s+3f_r (IMF3), f_s+4f_r (IMF3), f_s+5f_r (IMF3), f_s+6f_r (IMF3), f_s+7f_r (IMF3), f_s+5f_r (IMF4), f_s+f_o (IMF4), f_s+f_i (IMF4), f_s (IMF5), f_s-f_i (IMF5), f_i (IMF5), f_o (IMF5), f_r (IMF6), f_s-f_o (IMF7), IMF4 average envelope, Total: 21	PSH, f_s+14f_r , f_s+13f_r , f_s+12f_r , f_s+10f_r , f_s+2f_r , f_s+3f_r , f_s+4f_r , f_s+5f_r , f_s+6f_r , f_s+7f_r , f_s+f_o , f_s+f_i , f_s , f_i , f_o , f_r . Total: 19	PSH (D3), f_s+14f_r (D4), f_s+13f_r (D4), f_s+12f_r (D4), f_s+10f_r (D4), f_s+2f_r (A5), f_s+3f_r (A5), f_s+4f_r (D5), f_s+5f_r (D5), f_s+6f_r (D5), f_s+7f_r (D5), f_s+f_o (D5), f_s-f_i (A5), f_s+f_i (D5), f_o (A5), f_s+f_i (A5), f_s-f_i (A5), f_o (A5), f_r (A5), Total: 19

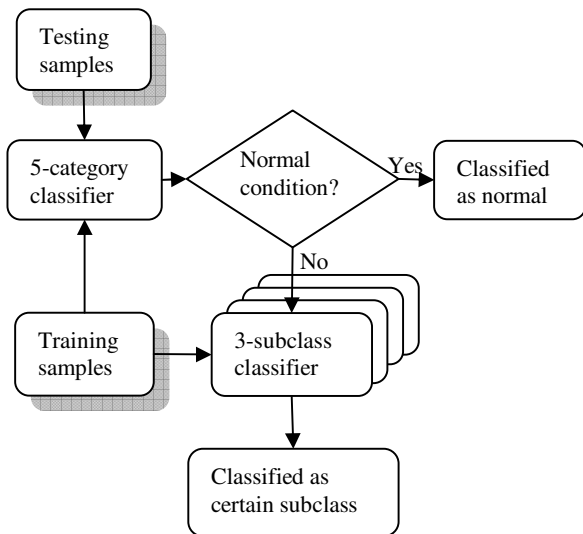


Fig. 6 Two-stage classifier processing structure

V. DATA ANALYSIS AND RESULTS

The Principal Slot Harmonic (PSH) can be calculated from equation 14. Since the rotor of the induction motor in this study has 46 bars, the PSH frequency is approximately 979.8 Hz. The opposite bearing is SKF bearing of series 6206, a deep groove ball bearing. There are 9 balls in the bearing. The contact angle is 0° . The ball diameter is 9.525mm and the pitch diameter is 46mm. The inner/outer race fault characteristic frequencies are 108.63Hz (equation 11) and 71.36 Hz (equation 10) respectively. The ball spin frequency is 46.22 Hz (equation 12). These features are used in the various classifiers. The three classifiers used are Naïve Bayesian (NB) classifier, k-Nearest Neighbor (k-NN) classifier and feed-forward back propagation Artificial Neural Network (ANN). The results are shown below.

1. Results of First Stage 5-Category Classification

For 5-category classification, 180 trials of each category are randomly selected as training data, and the remaining 180 trials are used as testing data. Table 3 lists the 5-category classifier results using only one of these sensors in the experiment. The microphone sensor itself can achieve 88.6% correct classification rate. Vibration sensor can only achieve 72.7% correct classification rate. This could be caused by the low sampling rate of vibration sensor and fewer features. The current sensor shows better performance than the vibration sensor in all three classifiers. Two microphones give similar classification rate results. From this table of results, none of the sensors individually can achieve a performance that is higher than 90% correct classification rate.

Because of the low classification accuracy, multiple sensors are necessary. From the vibration sensor results, the performance using HHT features is much better than using FFT and DWT features. Given the large number of trials (180 trials for each category) in the testing process, the difference (about 10%) is unlikely due to the chance error. From the current and microphone sensor results, the performance using HHT features is slightly worse than using FFT features. The performance using DWT features doesn't show any advantage. In order to achieve higher performance by using multiple sensor features, the HHT features from the vibration sensor and FFT features from current and microphone sensors are used in the feature level sensor fusion.

Table 3. Correct Classification Rate Using One Sensor

Classifier \ Sensor		Accelerometer	Current probe	Microphone 1	Microphone 2
		NB (%)	HHT: 60.7	59.5	72.9
	FFT	52.1	62.0	76.3	73.9
	DWT	48.9	57.2	69.1	68.7
k-NN (%)	HHT	72.7	68.5	81.7	87.1
	FFT	57.6	73.5	86.6	88.5
	DWT	51.5	58.3	73.7	71.9
ANN (%)	HHT	70.5	71.1	85.2	87.5
	FFT	55.3	71.8	82.2	88.6
	DWT	53.8	62.0	73.5	73.5

Table 4 shows the results tested using features from two sensors. The features from different sensors are simply accumulated in a feature vector (this is called feature level sensor fusion). The performance is greatly improved by using two sensor features. All the classification performance exceeds 90%. Although all the performances that involve microphone 2 are superior in Table 4 and the highest performance of single sensor in Table 3 is microphone 2, it does not mean that the performance is related to the position of the microphone tested here. To test the hypothesis that the position of the microphone 2 is responsible for its superior performance, the two microphones were interchanged so that microphone 1 now occupied the position of microphone 2 and vice versa. The results showed that it was the specific microphone hardware that contributed to its better performance, and not its location. Table 4 shows the results of best combination of two sensor features which the combination of two microphone sensors. The performance can be increased to 96.3% correct classification rate using ANN classifier. The other two classifiers also have high classification performance.

Table 4. Classification Results Using Two Sensors

Sensors*	Correct Classification Rate (%)		
	NB	k-NN	ANN
ACC + CP	76.9	89.2	90.3
ACC + Mic1	84.5	88.9	90.7
ACC+ Mic2	85.3	90.2	93.5
CP + Mic1	83.7	90.8	92.6
CP + Mic2	81.9	92.7	94.3
Mic1 + Mic2	83.7	91.7	96.3

*ACC: accelerometer; CP: Current Probe; Mic: Microphone

Table 5. Classification Results Using All Sensors

Sensors	Correct Classification Rate (%)		
	NB	k-NN	ANN
ACC + CP + Mic1	88.7	94	94.6
ACC+CP + Mic2	91.9	96.8	97.1
ACC+Mic1 + Mic2	88.5	92.3	96.0
CP+Mic1+Mic2	87.6	94.3	96.4
ACC+CP + Mic1+Mic2	95.7	97.0	97.9

Table 5 lists the classification results using all combinations of three sensors' features and all sensors' features. The performance of all combinations are higher than most of two sensor results. Almost all the classification performances exceed 95%. Among the combinations of three sensors' features, Microphone 2, vibration and current sensor give the highest performance. With all sensors used, the performance can achieve 97.9% correct classification rate using ANN classifier and all the classifiers give the performance above 95% correct classification rate. The higher performance of the first stage result, the higher the final classification rate of the system. Therefore, we should use all the sensors' features for the first stage classification.

2. Results of Second Stage Subclass Classification

In the 2nd stage classification, every category contains 3 subclasses except the normal condition. All the classification results above are an average of 10 cross validation tests since the training data sets are randomly selected from each condition of the training and testing data sets. Based on one simulation test results of the 1st stage classification using ANN classifier (Figure 7), all the correctly classified trials are used for the 2nd stage classification test. The final performance is simply the multiplication of these two stages' correct classification rate. Figure 7 shows the confusion matrix of the 1st stage

5-category classification results. A confusion matrix contains information about targeted and predicted classifications done by a classification system.

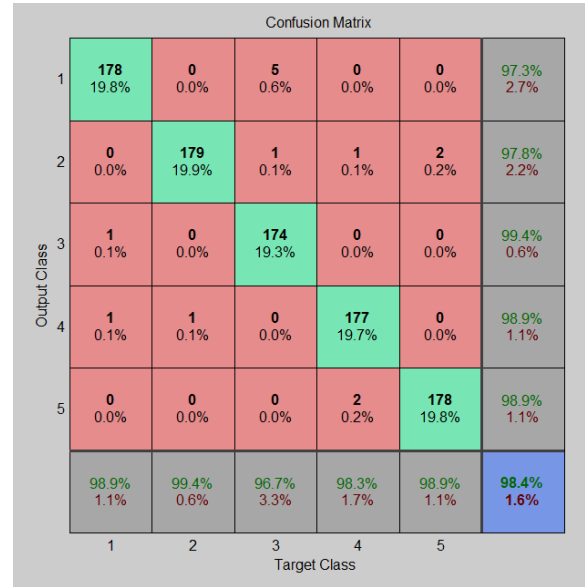


Fig. 7 Confusion matrix of ANN for 5-category classification using all sensors' features

In this case, each class has 180 testing trials. Class 1 to 5 represents two-fault condition, unbalanced stator winding resistance, air-gap eccentricity, damaged bearings and normal condition respectively. To read it vertically, for instance, there are 178 trials are correctly classified as class 1, one trial of class 1 is wrongly classified as class 3 and one trial of class 1 is wrongly classified as class 4. To read it horizontally, 5 trials of class 3 are wrongly classified as class 1. The last row shows the correct classification rate of each category in the 1st stage. The total of 900 testing trials in the 1st stage classification has the final performance of 98.4% correct classification rate. In the 2nd stage, all the training trials are used again in the subclass classifiers.

For 3-subclass classification, 60 trials of each class are used as training data, and the remaining 60 trials are used as testing data. Only the correct classified testing trials are evaluated in the subclass classifiers because there is no chance of correct classification at the second stage when the first stage classification is incorrect. Table 6 lists the results of the test finished for both 1st stage and 2nd stage classification. All the features from different sensors are used in the 2nd stage subclass classifiers. For simplicity the classifiers chose here are NB classifiers. Almost all the 2nd stage classification performance of this test has 100% correct classification rate. The final performance is about the same as the 1st stage performance.

Table 6. Final performance all conditions

	two-fault condition			unbalanced stator winding resistance				air-gap eccentricity			damaged bearing			normal condition
1st stage correct classification rate	98.9			99.4				96.7			98.3			98.9
2nd stage correct classification rate	98.3	98.3	100	100	100	100	100	100	100	100	100	100	100	
final performance	97.2	97.2	98.9	99.4	99.4	99.4	96.7	96.7	96.7	98.3	98.3	98.3	98.9	

VI. CONCLUSIONS

This paper described the empirical mode decomposition based method for the detection of multiple faults in induction motors. Three two-fault conditions are studied 1) Air-gap eccentricity with defective inner race in bearings 2) Air-gap eccentricity with defective outer race in bearings 3) Air-gap eccentricity with unbalanced winding resistance. The experiments are conducted under no-fault, single fault and multiple faults condition. The results demonstrate the effectiveness of using intrinsic mode functions in Hilbert-Huang transform to construct vibration sensor features for classification. However, no single sensor was able to achieve a high enough classification accuracy. Multiple sensors were required to enable reliable classification.

Due to the large number of classes, a two stage classification system is designed to solve the problem. Both HHT features of vibration sensor and FFT features of current and microphone sensors are used for classification. The first stage contains five categories and the second stage contains 3 subclasses for each faulty category. High classification accuracy is achieved by using multiple sensors and both HHT and FFT features.

This system can be easily extended by including additional category or sub-classes. In this study, only three combinations of two-fault conditions are trained in the system. More combinations can be studied and the three-fault condition can be included as an additional category in the future. The limitation of this system is the requirement of numerous experiments for each fault type. Furthermore the experiments were conducted in discrete steps. For example, three discrete types of air-gap eccentricity are simulated and validated. Motor faults usually occur gradually and thus, further experiments that can simulate continuous development of faults such as air-gap eccentricity are needed to verify the generalizability of the algorithms to intermediate stages of fault development.

ACKNOWLEDGEMENTS

The authors would like to thank Wallace Brithinee, Donald Brithinee and Bill Butek of Brithinee Electric Inc. located in Colton, California, for their support with equipment and expertise.

REFERENCES

- [1] J. R. Cameron, W. T. Thomson, and A. B. Dow, "Vibration and current monitoring for detecting airgap eccentricity in large induction motors," *Electric Power Applications, IEE Proceedings B*, vol. 133, pp. 155-163, 1986.
- [2] D. G. Dorrell, W. T. Thomson, and S. Roach, "Analysis of airgap flux, current, and vibration signals as a function of the combination of static and dynamic airgap eccentricity in 3-phase induction motors," *Industry Applications, IEEE Transactions on*, vol. 33, pp. 24-34, 1997.
- [3] Z. Wei, T. G. Habetler, and R. G. Harley, "Bearing Condition Monitoring Methods for Electric Machines: A General Review," in *Diagnostics for Electric Machines, Power Electronics and Drives, 2007. SDEMPED 2007. IEEE International Symposium on*, 2007, p. 3.
- [4] B. Li, M. Y. Chow, Y. Tipsuwan, and J. C. Hung, "Neural-network-based motor rolling bearing fault diagnosis," *Industrial Electronics, IEEE Transactions on*, vol. 47, pp. 1060-1069, 2000.
- [5] R. R. Schoen, T. G. Habetler, F. Kamran, and R. G. A. B. R. G. Bartfield, "Motor bearing damage detection using stator current monitoring," *Industry Applications, IEEE Transactions on*, vol. 31, p. 1274, 1995.
- [6] Z. K. Peng, P. W. Tse, and F. L. Chu, "A comparison study of improved Hilbert-Huang transform and wavelet transform: Application to fault diagnosis for rolling bearing," *Mechanical Systems and Signal Processing*, vol. 19, pp. 974-

988, 2005.

- [7] W. G. Zanardelli, E. G. Strangas, and S. Aviyente, "Identification of Intermittent Electrical and Mechanical Faults in Permanent-Magnet AC Drives Based on Time-Frequency Analysis," *Industry Applications, IEEE Transactions on*, vol. 43, p. 971, 2007.
- [8] W. G. Zanardelli, E. G. Strangas, H. K. Khalil, and J. M. Miller, "Wavelet-based methods for the prognosis of mechanical and electrical failures in electric motors," *Mechanical Systems and Signal Processing*, vol. 19, p. 411, 2005.
- [9] V. K. Rai and A. R. Mohanty, "Bearing fault diagnosis using FFT of intrinsic mode functions in Hilbert-Huang transform," *Mechanical Systems and Signal Processing*, vol. 21, pp. 2607-2615, 2007.
- [10] B. Liu, S. Riemenschneider, and Y. Xu, "Gearbox fault diagnosis using empirical mode decomposition and Hilbert spectrum," *Mechanical Systems and Signal Processing*, vol. 20, pp. 718-734, 2006.
- [11] L. Hui and Z. Haiqi, "Bearing Fault Detection Using Envelope Spectrum Based on EMD and TKEO," in *Fuzzy Systems and Knowledge Discovery, 2008. FSKD '08. Fifth International Conference on*, 2008, pp. 142-146.
- [12] N. E. Huang, Z. Shen, S. R. Long, M. L. C. Wu, H. H. Shih, Q. N. Zheng, N. C. Yen, C. C. Tung, and H. H. Liu, "The empirical mode decomposition and the Hilbert spectrum for nonlinear and non-stationary time series analysis," *Proceedings of the Royal Society of London Series a-Mathematical Physical and Engineering Sciences*, vol. 454, pp. 903-995, Mar 1998.
- [13] N. Huang, M. Wu, S. Long, S. Shen, W. Qu, P. Gloersen, and K. Fan, "A confidence limit for the empirical mode decomposition and Hilbert spectral analysis," *Royal Society of London Proceedings Series A*, vol. 459, pp. 2317-2345, 2003.
- [14] S. Hahn, *Hilbert transforms in signal processing*: Artech House Publishers, 1996.
- [15] S. G. Mallat, "A theory for multiresolution signal decomposition: the wavelet representation," *Pattern Analysis and Machine Intelligence, IEEE Transactions on*, vol. 11, pp. 674-693, 1989.
- [16] S. Nandi and H. A. Toliyat, "Condition monitoring and fault diagnosis of electrical machines-a review,"

in *Industry Applications Conference, 1999. Thirty-Fourth IAS Annual Meeting. Conference Record of the 1999 IEEE*, 1999, p. 197.

- [17] W. T. Thomson, "On-line MCSA to diagnose shorted turns in low voltage stator windings of 3-phase induction motors prior to failure," in *Electric Machines and Drives Conference, 2001. IEMDC 2001. IEEE International*, 2001, pp. 891-898.
- [18] M. Rashid, *Power Electronics Handbook: Devices, Circuits, And Applications*: Academic Press, 2006.
- [19] S. Prabhakar, A. R. Mohanty, and A. S. Sekhar, "Application of discrete wavelet transform for detection of ball bearing race faults," *Tribology International*, vol. 35, pp. 793-800, 2002.

Xin Xue is a graduate student in the Department of Mechanical Engineering at the University of California, Riverside. Her research interests include condition monitoring, sensor networks, sensor fusion, energy harvesting. She received her BS in mechanics and engineering science from Fudan University. Contact her at A108 Bourns Hall, Univ. of California, Riverside, Riverside, CA 92507, xxue@engr.ucr.edu

V. Sundararajan is a faculty member in the Department of Mechanical Engineering at the University of California, Riverside. His research interests include sensor networks, environmental monitoring, energy harvesting, computational geometry, collaborative processing, and manufacturing systems. He received his MS and PhD in mechanical engineering from UC Berkeley. Contact him at A317 Bourns Hall, Univ. of California, Riverside, Riverside, CA 92521; vsundar@engr.ucr.edu